




Structural features of solid-solid phase transitions and lattice dynamics in U_3O_8

Andrew Miskowicz ^{*}, Tyler Spano , Rodney Hunt, Ashley E. Shields , and J. L. Niedziela
Oak Ridge National Laboratory, Oak Ridge, Tennessee 37831, USA

Sarah Finkeldei

Department of Chemistry, University of California, Irvine, Irvine, California 92617, USA



(Received 29 April 2020; revised 20 July 2020; accepted 3 September 2020; published 29 September 2020)

Triuranium octoxide (U_3O_8) undergoes an orthorhombic to hexagonal structural phase transition near $T_s = 305^\circ\text{C}$, and a separate nonstructural phase transition at $T_c = 210^\circ\text{C}$. The later transition has previously been associated with temperature-induced fluctuations in the uranium oxidation state. A discontinuity in the slope of electrical conductivity versus temperature measurement at 210°C has supported this idea. The orthorhombic phase has three crystallographic sites in two distinct oxidation configurations [2 U(V) and 1 U(VI)], whereas the hexagonal phase has one distinct uranium site. High-resolution x-ray diffraction measurements eliminate the possibility of superlattice Bragg reflections to less than $0.2 e^-$ scattering power and U_3O_8 is not metallic; consequently, the presence of oxidation fluctuations is required for charge balancing. Interestingly, the order-to-disorder transition occurs at a much lower temperature than the structural transition. Using temperature-dependent x-ray diffraction and Raman spectroscopy, we show anisotropic lattice expansion in the in-plane b and c lattice constants. A specific discontinuity in the temperature derivatives of the b and c lattice constants are the first reported structural signatures of the order-to-disorder transition, suggestive of a change in local U–O coordination. Phonon frequencies of U_3O_8 measured by Raman spectroscopy show significant temperature-dependent dynamics. Redshifting of several modes between 40 and 300°C cannot be explained by unit cell expansion alone because the unit cell volume *decreases* in this region. Instead, we show that phonon frequencies are highly correlated with the anisotropic lattice expansion/contraction along specific crystallographic directions.

DOI: [10.1103/PhysRevMaterials.4.093610](https://doi.org/10.1103/PhysRevMaterials.4.093610)

I. INTRODUCTION

Owing to its exceptional chemical stability, calcination of many uranium compounds yields triuranium octoxide (U_3O_8) [1]. As a stable oxide, U_3O_8 is of obvious technological interest in the fuel cycle. As a specific example, the oxidation of UO_2 occurs along the [111] lattice plane and results in a significant expansion of the lattice, and spallation of material is a real concern in fuel applications of UO_2 [2].

Below 300°C , U_3O_8 is orthorhombic ($Z = 2$, $Amm2$). It has a singly degenerate site at the 2a position and a doubly degenerate site at the 4d position [3]. Collectively, the oxidation state in the orthorhombic phase is determined from K-edge photoemission studies as $2U(V) + U(VI)$ [4,5]. Above 300°C , the $P\bar{6}2m$ phase is $Z = 1$ with a triply degenerate U site at $3f$ [6–9]. These structures are nearly isomorphic as shown in Fig. 1, and the hexagonal phase is realized when the U sites are structurally degenerate.

A foundational measurement is the heat capacity determination first performed by Girdhar and Westrum and expanded by Momin *et al.* and Inaba *et al.* on stoichiometric U_3O_8 [10–12]. In those data, Inaba *et al.* observed three λ -type anomalies in the heat capacity at 210 , 295 , and 577°C . To

explain the 210°C anomaly, they proposed an order-to-disorder transition wherein the uranium oxidation transitions from distinct U(V) and U(VI) to a disordered configuration. This hypothesis is supported by conductivity measurements that show a discontinuity at the same temperature [13]. The 295°C anomaly is associated with the orthorhombic to hexagonal structural transition. But the fact that the uranium oxidation state could become disordered *before* the structural transition has two fascinating implications. First, in the region 210 – 295°C , a disordered uranium valence would exist in a structure with distinct crystallographic sites. In that case, the valence configuration cannot be $2 U(V) + 1 U(VI)$ because it is disordered, but what other configuration could match the crystal structure? Second, this fact would imply that the onset of electronic degeneracy is *not* the driving force for the transition into the hexagonal phase.

At the time, no x-ray or neutron diffraction data indicated a structural change associated with this order-to-disorder transition. If the 210°C heat capacity anomaly is indeed caused by the onset of an order-to-disorder transition of the uranium valence, could this fluctuating uranium valence explain the electronic configuration in the hexagonal phase, wherein only one triply degenerate uranium site must balance $16 e^-$ of charge? In addition, are there static structural signatures of the fluctuating valence or is it dynamically stabilized, perhaps by phonons?

^{*}Corresponding author: miskowiczaj@ornl.gov

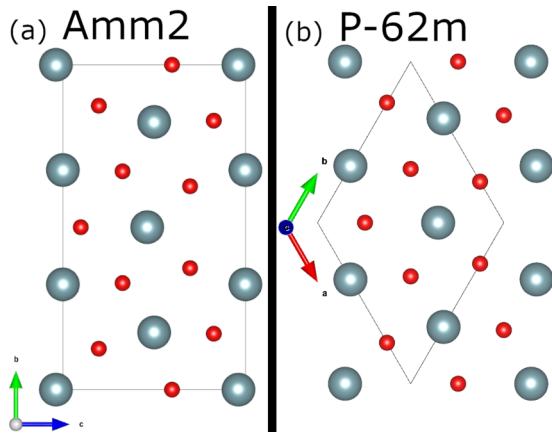


FIG. 1. Structure of α - U_3O_8 in the (a) $Amm2$ phase and (b) in $P\bar{6}2m$. The $Amm2$ phase is present below 300°C and the $P\bar{6}2m$ above. They are, however, nearly isomorphous. An important difference is the presence of two crystallographically distinct U atoms in the $Amm2$ phase [2 U(V) + 1 U(VI)], but only one in the higher symmetry phase. The electronic structure in the $P\bar{6}2m$ phase is unknown. Because it is weakly semiconducting, $-16/3 e^-$ of charge must be distributed across a single lattice site.

Depending on the nature of the valence disorder in the hexagonal phase, we may expect differences in the structure itself. Several possible descriptions of disorder could exist and fit within the existing data. One, the charges could actually be ordered on longer lengthscales, such that ordering presents itself at the hexagonal superlattice positions $([0.5, 0, 0])$ or $[0.5, 0.5, 0]$, for example) and whose x-ray scattering power would be on the order of $1-2 e^-$. Two, the uranium valence is time-independent (or equivalently, slowly varying), wherein distinct U(V) and U(VI) states exist. Short-range ordering may be present in this case, showing a preference for neighboring sites to have opposite charge, but not long-range ordering, and it may be observable with high-resolution x-ray pair distribution function measurements. Three, a time-dependent, fluctuating U valence is present, wherein excess electrons hop from site to site. The difference between time-independent and time-dependent valence configurations is a matter of electron hopping timescales, but their structural signatures will depend on those timescales. Last, a final possibility is that hexagonal U_3O_8 is metallic, but conductivity measurements show semiconducting behavior at all measured temperatures [13,14].

Given the relevant temperatures ($210-300^\circ\text{C}$), the possibility of phonon interactions stabilizing a disordered uranium valence should be considered. To that end, we are investigating in parallel the lattice dynamics via Raman spectroscopy and the structure via x-ray diffraction. U_3O_8 has 63 optical phonons (all Raman active) and a distinct spectrum that makes it possible to distinguish from other species in micro-Raman measurements [15–18]. Owing to its strong activity, Raman spectroscopy is a useful technique for investigating the lattice dynamics in this material. Many investigators described similar features of the Raman spectra: a triplet of modes in the $320-480 \text{ cm}^{-1}$ region, several modes between 100 and 250 cm^{-1} , and occasionally a single mode at 810 cm^{-1} . In

particular, the triplet modes are the most intense and most reliable indicators of the presence of U_3O_8 , but they are broad ($\approx 30 \text{ cm}^{-1}$ FWHM). Broadening of this magnitude, especially in a spectra that demonstrates other modes without significant broadening, is not due to crystalline confinement effects [19]. Instead, the most likely cause of this broadening is electron–phonon interactions.

We will present temperature-dependent measurements of the x-ray diffraction pattern of stoichiometric U_3O_8 with a specific aim to investigate possible superlattice reflections, as well as possible structural signatures of the 210°C thermal peak. At the same time, the temperature-dependent lattice dynamics will be presented, and their unusual temperature behavior will be discussed.

II. MATERIALS AND METHODS

Triuranium octoxide was produced by calcination of natural isotopic composition UO_2 . Specimens of UO_2 were heated to 700°C for 180 m in air in a Thermolyne 47900 furnace as previously described [18]. The measured mass increase corresponded to a final composition of $\text{U}_3\text{O}_{7.98}$ ($\approx 99\%$ oxidized from UO_2).

X-ray diffraction measurements were collected on powders of U_3O_8 across a range of temperatures from 30 to 500°C in increments of 5°C , except between 180 and 230°C where the increment was 3°C . Between measurements the temperature was increased at a rate of $1^\circ\text{C}/\text{min}$ with no additional equilibration time. Measurements were collected from $2\theta = [10, 60]$ deg with an area detector (a total count time of approximately 1 h per dataset) using a Cu anode ($\lambda = 1.5406 \text{ \AA}$). Silicon line position standard (NIST SRM 640e) powder was mixed with the U_3O_8 directly, and a θ -dependent correction polynomial was applied to the collected data based on the known temperature dependence of Si. Sequential Rietveld analysis was performed with GSAS-II [20]. All lattice constants were determined using the $Amm2$ space group, even above 300°C , as $P\bar{6}2m$ is a high-symmetry case of $Amm2$.

Raman spectra were collected on a Renishaw inVia micro-Raman spectrometer with a 785-nm laser. The powder sample was loaded in a Linkam DSC600 temperature-controlled stage and imaged with a $50\times$ objective with a 8.2 mm working length (Leica). The estimated peak power density is $< 100 \text{ W}/\text{cm}^2$ on sample. Spectral changes were noted at higher power levels. An increase in fluorescence background was observed with the 785-nm laser at higher powers, and shifts in width and position of certain peaks were noted. Similar changes were observed at high power densities with 532- and 633-nm lasers, as well. We note that exposing the specimen to high power ($> 100 \text{ W}/\text{cm}^2$) for several seconds results in some physical changes (such as reorientation of particles presumably due to thermal expansion), but no ostensible chemical change as indicated by reproducibility of the spectrum when measuring the same region at lower power after exposure. Nevertheless, the very low power density is preferable to ensure that the local temperature is constant. To verify that the observed spectrum did not correspond to a locally higher temperature, a measurement with $< 1 \text{ W}/\text{cm}^2$ at room temperature was collected and was

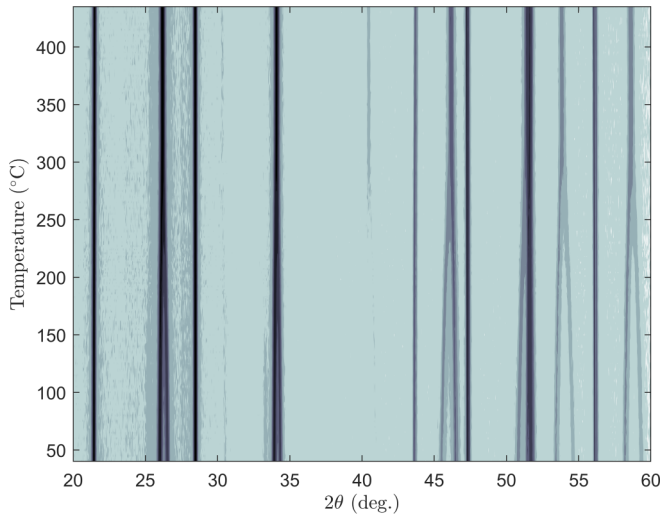


FIG. 2. X-ray diffraction pattern of U₃O₈ with NIST SRM 640e (Si line position standard) (color scale: log x-ray counts) as a function of temperature in the range 20–60 2θ as acquired with CuK α radiation ($\lambda = 1.5406 \text{ \AA}$). Data are collected every 5 °C, except between 180 and 230 °C, where the data are collected every 3 °C. Total count time for each scan was ≈ 1 hr.

indiscernible from the $< 100 \text{ W/cm}^2$ data presented below. For temperature-dependent measurements, spectra were collected every 10 °C between 30 and 400 °C. Between measurements, the stage temperature was increased at a rate of 5 °C/min and stabilized for 2 min before data collection. Importantly, a notch filter with a 60 cm^{-1} blocking width was inserted before the detector, providing reliable spectral intensity down to 45 cm^{-1} . Scattered light was analyzed with a 1200 l/mm grating providing an approximate spectral resolution of 3 cm^{-1} .

The sequential fitting method in a custom curve fitting environment (PEAKFITGUI) based on the LMFIT module was used to perform multiplex fitting [21,22]. An asymmetric least-squares algorithm with $p = 100\,000$ and $\lambda = 0.015$ is employed to determine the background contribution and subtracted from each spectrum prior to fitting [23].

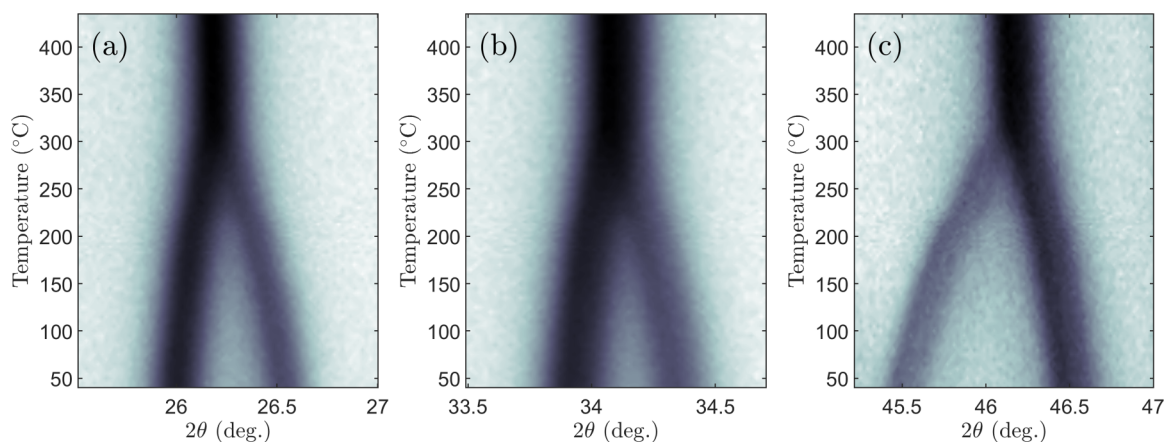


FIG. 3. X-ray diffraction patterns of U₃O₈ (color scale: log x-ray counts) for the (a) [031]/[002] \rightarrow [110], (b) [131]/[102] \rightarrow [111], and (c) [060]/[033] \rightarrow [300] as a function of temperature, showing a simultaneous convergence of peaks near 300 °C.

TABLE I. Refined lattice constants of α -U₃O₈.

T °C	Ref.	a Å	b Å	c Å	Vol. Å ³
40	This work	4.147(3)	11.955(3)	6.721(3)	333.2(5)
23	Ackermann[3]	4.149	11.961	6.726	333.785
23	Loopstra[24]	4.148	11.968	6.717	333.453
355	This work	4.140(6)	11.817(5)	6.799(5)	332.7(1)
358	Ackermann[3]	4.136	11.804	6.815	332.717

III. RESULTS AND ANALYSIS

A. X-ray diffraction

In Fig. 2 the x-ray diffraction pattern of U₃O₈ from 40 to 450 °C is shown. As noted in previous studies, the solid–solid phase transition from $Amm2$ to $P\bar{6}2m$ is evidenced by the condensation of nondegenerate b and c lattice constants into a single a/b lattice constant in the hexagonal phase, particularly visible near $2\theta = 26^\circ$ where the [031] and [002] Bragg peaks converge into the [110] peak [3]. (We use the assignment of b and c to in-plane lattice constants in $Amm2$ and a and b for in-plane lattice constants in $P\bar{6}2m$ as per the original reports [3,24,25].)

This convergence can be seen in more detail in Fig. 3, which shows three pairs of Bragg peaks merging near 300 °C. As Fig. 3(c) shows, the convergence is affected by both the decrease in the orthorhombic b lattice constant and an increase in c lattice constant.

Figure 4 shows the expansion of c and contraction of b lattice constants with increasing temperature in more detail. Table I provides a comparison of with previously measured lattice constants. The out-of-plane lattice constant (a) decreases with temperature, and the in-plane lattice constants converges to the hexagonal value ($b/c = 1.732$). Overall, the unit cell volume reaches a minimum near the $Amm2 \rightarrow P\bar{6}2m$ phase transition and then increases above 350 °C. Lattice constants and unit cell volumes are in good agreement with previous results at both ambient and elevated temperature—no major discrepancies are noted. Because the lattice constants reported here are pinned against a standard material (NIST SRM 640e),

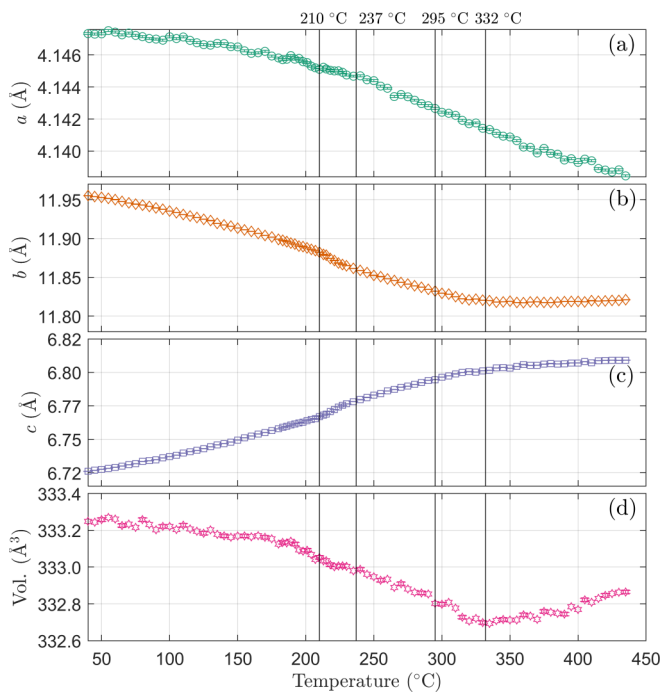


FIG. 4. Lattice constants (a) a , (b) b , (c) c , and (d) unit cell volume as a function of temperature. Qualitative agreement is observed with all components to previous work. In particular, the decrease in both out-of-plane lattice constant a and unit cell volume from 210 to 300 °C was observed by Ackermann *et al.* [3]. The vertical lines at 210, 237, 295, and 332 °C are the onset and offset temperatures of two calorimetric peaks identified by Inaba *et al.*, which were identified by those authors as a uranium valence order-to-disorder transition and the structural transition from $Amm2$ to $P\bar{6}2m$ [12].

their uncertainty is commensurate with the uncertainty of the standard and the resolution of the instrument.

Figure 5 plots the ratio of b and c lattice constants as a function of temperature, as well as its derivative. Superimposed in Fig. 5 are the onset and offset temperatures of two calorimetric peaks identified by Inaba *et al.* beginning at 210 and 295 °C [12]. In addition to showing the expected behavior (converging to the hexagonal value), a discontinuity in the derivative of b/c is observed precisely near 210–237 °C, commensurate with the calorimetric peak. A closer examination of Figs. 4(b) and 4(c) shows that discontinuities in the derivatives of b and c themselves are also present.

As discussed earlier, a peak in the heat capacity at 210 °C is an important feature of that quantity, and it has been suggested to be related to the onset of disorder in the uranium valence. No specific structural signature has been identified in association with this temperature. Figures 4 and 5 clearly show a discontinuity in the in-plane lattice constants at the same temperature as the peak in heat capacity. Because the out-of-plane a lattice constant does not exhibit any qualitative changes in this region, the calorimetric peak is associated with changes to the in-plane U–O coordination.

The second calorimetric peak begins at 295 °C, which, based on Figs. 2 and 3, corresponds to the completion of the $Amm2 \rightarrow P\bar{6}2m$ phase transition. In the same way, 295 °C corresponds to a second discontinuity in the derivative of

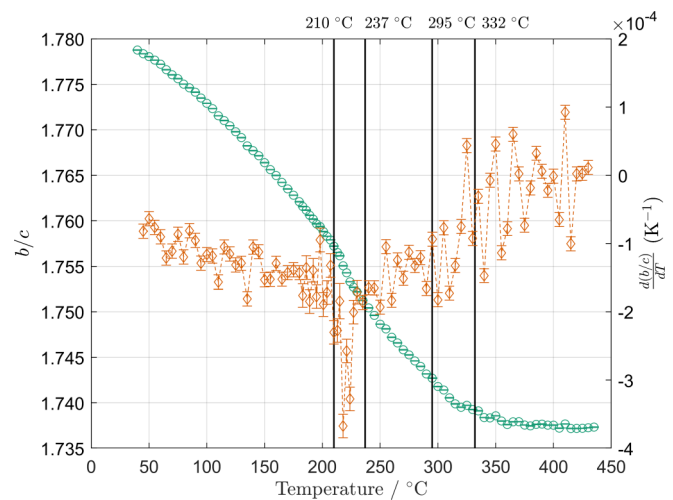


FIG. 5. Ratio of b to c lattice constant as a function of temperature (green points, left axis) and its derivative (red points, right axis). The vertical lines at 210, 237, 295, and 332 °C are the onset and offset temperatures of two calorimetric peaks identified by Inaba *et al.*, which were identified by those authors as a uranium valence order-to-disorder transition and the structural transition from $Amm2$ to $P\bar{6}2m$ [12].

b/c (Fig. 5) that ends approximately near 332 °C, although these data are much noisier. With reference to Fig. 4, the unit cell volume clearly reaches a minimum value near the offset temperature of the heat capacity peak.

Finally, as discussed in the introductory remarks, one possible resolution of the incommensurateness of the U oxidation configuration with a crystal structure that only has one crystallographic site (as in $P\bar{6}2m$) would be a long-range charge ordering, given by the distribution of excess electrons into neighboring unit cells in the hexagonal structure. In essence, the low-temperature orthorhombic structure represents exactly this configuration, but with a commensurate rearrangement of the ionic sublattice, evidenced by the breaking of the (hexagonal) [110] degeneracy at low temperatures. But, if an electronic charge ordering occurs without a commensurate ionic rearrangement, the oxidation configuration could be stabilized by U atoms in neighboring unit cells having a different oxidation number. If this arrangement were ordered, it would give rise to superlattice Bragg reflections. If the ordering involved strictly electron rearrangements, its scattering power could be as little as $1 e^-$. If the ordering also involved the relatively weakly scattering O atoms, a $[0.5, 0, 0]$ Bragg peak may be stronger. To our knowledge, x-ray diffraction data in the superlattice region have not been reported.

In Fig. 6, the results of long scans collected over the superlattice region (where the hexagonal $[0.5\ 0\ 0]$ Bragg peak would be) are shown. The data were collected at 350 °C after being equilibrated for 1 h. Data were framed in 0.02 2θ steps, each collected for 120 s. After measurement, the sample holder (a zero-background silicon plate) was rinsed of U_3O_8 and measured under the same conditions and orientation. In total, each measurement represents 8.3 h of counting time, each point representing approximately 150 000 signal and background counts. Assuming a positive identification

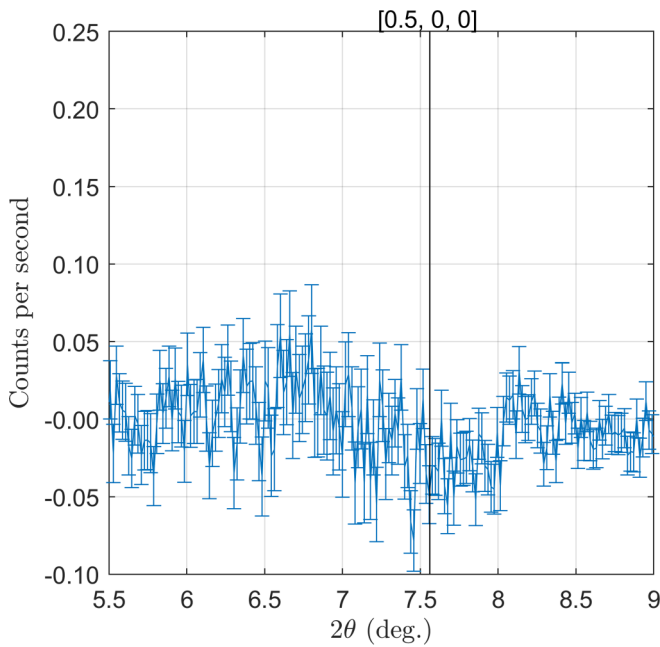


FIG. 6. Background subtracted long scan of U_3O_8 over the hexagonal $[0.5, 0, 0]$ Bragg peak position collected at 350°C . The specimen was heated to 350°C , held for 1 h, and data were collected for 120 s per 0.02° 2θ from $2\theta = 5$ – 10° (8.3 h total counting time). A background measurement was collected on the same zero-background silicon plate after rinsing the U_3O_8 and positioning identically in the instrument. Each point is the difference between approximately 1.5×10^5 counts. The data show no superlattice reflections associated with long-range, time-averaged charge ordering in the hexagonal phase.

criterion that peak height be larger than twice the standard deviation in the noise, the minimum peak height of an observable Bragg peak would scatter 0.1738 counts per second. In Fig. 3, the Bragg peak height of the $[110]$ hexagonal peak is 50.49 counts per second and corresponds to a scattering power of $\approx 58 e^-$. Therefore a Bragg peak height of 0.1738 corresponds to a scattering power of $\approx 0.2 e^-$. Because we observed no significant scattering in Fig. 6, we conclude that a long-range, time-averaged charge ordering along the hexagonal axes (at $[0.5, 0, 0]$) cannot be greater than $0.2 e^-$ in magnitude. The $([1/3, 1/3, 0])$ Bragg position at $2\theta = 8.64^\circ$ can also be eliminated at this level. Based on the same criteria with data collected in Fig. 2 at 350°C , any superlattice reflections at $[0.5, 0.5, 0]$ ($2\theta = 13.1^\circ$) are no stronger than $0.53 e^-$. We cannot exclude superlattice reflections corresponding to d -spacing larger than 16 \AA , which is outside the range of our measurement, nor can we exclude time-independent, disordered charge configurations. But Fig. 6 is strong evidence against the existence of a time-independent, ordered distribution of U(V) and U(VI) sites in the hexagonal phase.

B. Raman spectroscopy

In Fig. 7(a), high-resolution Raman spectra at room temperature show a center triplet of modes between 300 and 550 cm^{-1} , a sharp, strong mode located at 52 cm^{-1} , and a multiplet of modes between 60 and 180 cm^{-1} . By total

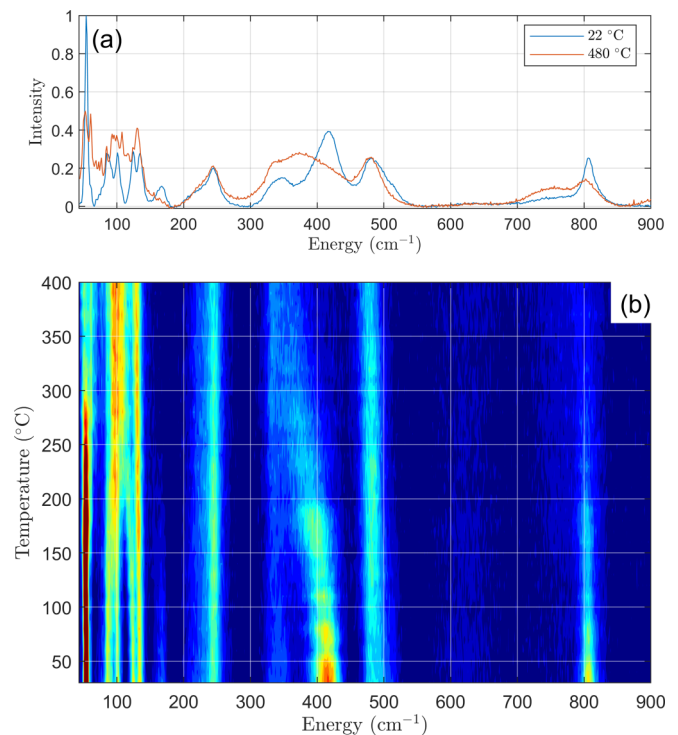


FIG. 7. High-resolution, background-subtracted Raman spectra of U_3O_8 collected at ambient temperature (22°C) and at high temperature (480°C) with (a) $\lambda = 785 \text{ nm}$. Main features include a triplet of modes between 300 and 550 cm^{-1} , a lower energy multiplet between 60 and 180 cm^{-1} , and a strong, narrow peak at 52 cm^{-1} . No discernible dispersive behavior was observed when measured with 532- and 633-nm lasers. We recently provided a full account of the ambient temperature Raman modes [18]. In panel (b), the temperature dependence between 30 and 400°C is shown (color scale: Raman counts). The most apparent feature with increasing temperature is the softening, broadening, and attenuation of the center band peak at 418 cm^{-1} (as measured at 22°C). Other notable features include the attenuation of the 804 and 52 cm^{-1} peaks, as well as some discernible shifting in the 60 – 180 cm^{-1} multiplet and the 485 cm^{-1} peak.

intensity, the triplet of modes near 400 cm^{-1} dominate, and these are the set that have previously been used to identify U_3O_8 [26]. However, for the purposes of identifying chemistry on the microscale, the presence of the 52 cm^{-1} mode is noteworthy because of its resolution-limited spectral width, a feature that improves its legibility in low intensity samples. We recently provided a more complete account of these features [18]. Notably, the triplet between 300 and 550 cm^{-1} can be decomposed into a septet with low count-rate uncertainty data, but it is also reasonably well described by three Gaussian lineshapes.

Figure 7(b) shows the background subtracted Raman spectra of U_3O_8 as a function of temperature, through the calorimetric and structural phase transitions. We note several qualitative features immediately. First, the center band mode starting at 418 cm^{-1} softens, broadens, and attenuates with increasing temperature. Hints of this peak remain even at 400°C , although significantly attenuated. Second, the 52 cm^{-1} peak is attenuated around 300°C , and the 804 cm^{-1} peak attenuates somewhat below 300°C . Third, at low

TABLE II. Calculated centers of mass at 30 and 400 °C for each vibrational band.

Band	Range	Band c.o.m.		Difference cm ⁻¹	Band Int.		Difference a.u.
		30 °C cm ⁻¹	400 °C cm ⁻¹		30 °C a.u.	400 °C a.u.	
1	[45–66]	54.2	55.8	1.6	1	0.57	-0.43
2	[68–185]	116.8	106.5	-10.3	1	1.24	0.24
3	[185–300]	236.4	239.0	2.6	1	0.87	-0.13
4	[300–440]	396.6	364.2	-32.4	1	0.54	-0.46
5	[440–542]	490.3	479.6	-10.7	1	0.89	-0.11
6	[542–708]	630.2	634.2	4.0	1	1.17	0.17
7	[708–870]	799.8	780.6	-19.3	1	0.74	-0.26

temperatures, four peaks at 87, 101, 124, and 134 cm⁻¹ are easily discernible, but a combination of mode shifting and attenuation leaves only two bands observable in this region above 300 °C. Although the background is increasing with temperature, these observations are probably not dependent on the details of the background subtraction, as is evidenced by the relative change in peak intensities (e.g., the 418 cm⁻¹ is attenuated, but the neighboring 492 cm⁻¹ peak remains strong).

We take two approaches to quantifying the Raman temperature dependence. First we present a “model-independent” method to quantify peak shifting based on the center-of-mass determination in spectral bands. Then, we will discuss the details of peak fitting for select regions of interest between 60–180 and 300–550 cm⁻¹, covering the two main multiplets.

C. Band center of mass

To quantify temperature dependence of the Raman spectra, each spectrum is binned into a set of “bands,” corresponding to a particular region of the spectrum. We calculated the band center of mass (c.o.m.) using the following equation:

$$C_i(T) = \frac{\int_{b_1}^{b_2} \omega I(\omega, T) d\omega}{\int_{b_1}^{b_2} I(\omega, T) d\omega}, \quad (1)$$

where b_1 and b_2 are the ranges of each band, ω is Raman shift, and $I(\omega, T)$ is the spectral intensity after background subtraction at each temperature. The c.o.m. is sensitive to shifts in location of spectral intensity (such as the primary shift in the 418 cm⁻¹ peak in Fig. 7) without relying on peak fitting algorithms. Band limits are selected by choosing values corresponding to minima between sets of peaks, but they are ultimately qualitative. Another quantity of interest is the band intensity, given by

$$S_i(T) = \int_{b_1}^{b_2} I(\omega, T) d\omega. \quad (2)$$

In Table II the band c.o.m. is tabulated both at 30 and 400 °C and plotted in Fig. 8 for all temperatures. Shifts in the band c.o.m. correspond to changes in the frequency of spectral intensity. Large negative shifts in c.o.m. are observed in the [300–440] cm⁻¹ band and the [708–870] cm⁻¹ band, with smaller shifts in bands 2 and 5 ([68–185] and [440–542] cm⁻¹). The remaining bands show slight increases in band intensity. Generally, phonon frequencies should decrease

with increasing temperature as a result of thermal expansion. However, in the *Amm2* phase of U₃O₈, the unit cell volume is *decreasing* in this temperature region as shown in Fig. 4. This unusual behavior can be explained by comparing the phonon frequencies to the c lattice constant instead as we discuss below.

In band 1, containing the sharp mode at 54 cm⁻¹, the single mode at 54 cm⁻¹ is clearly composed of two modes, especially at higher temperatures. Although the 54 cm⁻¹ mode becomes attenuated above 300 °C, the shoulder at 60 cm⁻¹ remains. Therefore, the increase in band c.o.m. is not attributable to a shift in mode frequency *per se* but to a decrease in the intensity of the 54 cm⁻¹ mode in particular. Overall, the intensity of this band is decreasing by 43% from 30 to 400 °C. In fact, all bands except for band 2 ([68–185 cm⁻¹]) are attenuated at higher temperature.

D. Peak fitting

For the subsets of modes in the 60–180 cm⁻¹ multiplet and 300–550 cm⁻¹ multiplet, it was possible to perform multipeak fitting to decompose the bands into their constituent parts. These regions were noted to be of special interest because the strong shifting of the band c.o.m. and relatively high intensity as identified in Fig. 8. Fitting was performed with the PEAKFITGUI package built on the LMFIT module, and results are tabulated in Table III [21,22]. Peaks are modeled with Gaussian functions

$$G(x) = \frac{A}{\sigma\sqrt{2\pi}} \exp[-(x - \mu)^2/2\sigma^2], \quad (3)$$

where A is the amplitude, μ is the center position, and σ is the Gaussian linewidth (full-width at half-maximum equal to 2.35σ). Alternative peak shapes were explored, including Lorentzian and pseudo-Voigt (weighted Gaussian and Lorentzian sum) lineshapes, but neither resulted in justifiable improvements in fit quality. The Akaike information criterion was used to differentiate peak shapes and justify the number of peaks included in the fit. Figures 9 and 10 plot the linewidth, center position, and intensity of the constituent peaks for the quartet (four peaks) and triplet (three peaks), respectively.

The two higher-energy peaks of the quartet (centered at 123 and 134 cm⁻¹ at 30 °C) show increasing linewidth associated with a decrease in phonon lifetime and decreasing frequency. Under normal circumstances of positive thermal

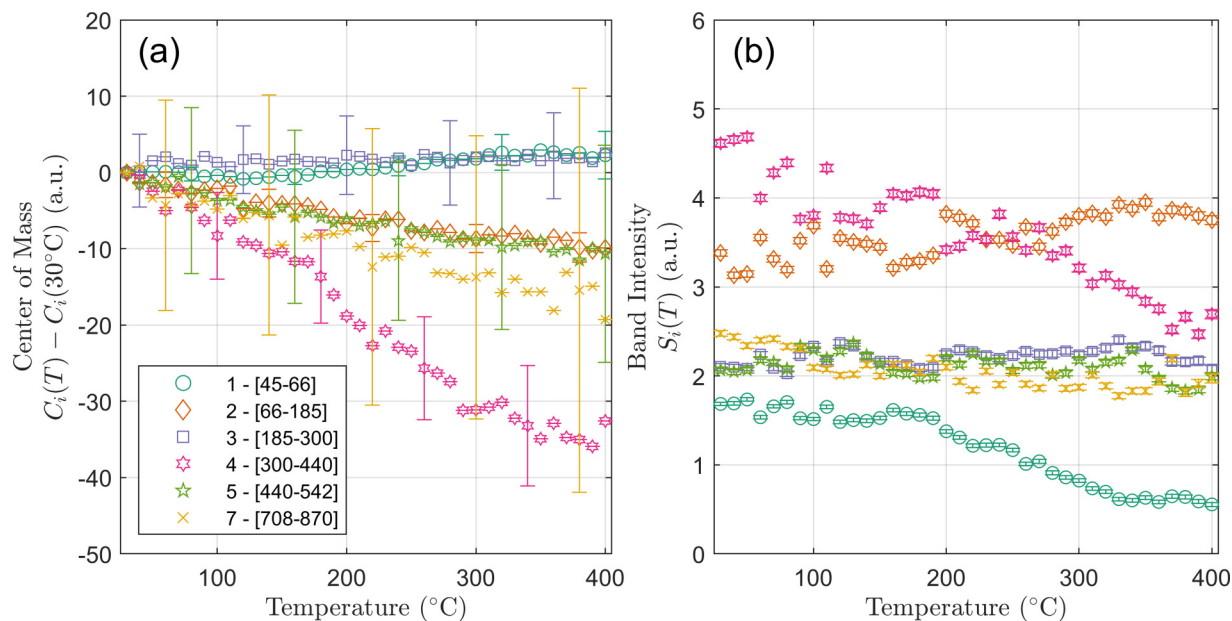


FIG. 8. Band center of mass $[C_i(T)$, c.o.m.] compared to c.o.m. at (a) 30°C and (b) band intensity $[S_i(T)]$ for all bands. The most significant shifts in band c.o.m. occur for band 4, corresponding to the $300\text{--}440\text{ cm}^{-1}$ region. This band also shows the most significant change in intensity. Bands 2, 5, and 7 are also shifting to lower energy with increasing temperature. The increase in band c.o.m. for band 1 can be attributed to the attenuation of the peak at 54 cm^{-1} with increasing temperature, not a shift *per se*, as can be seen by the attenuation of $S_2(T)$. Band 6 ($[542\text{--}708]$) contains a small background intensity and is excluded.

expansion, both of these behaviors are normal. However, the two low energy peaks at 87 and 101 cm^{-1} converge at 180°C . Above 180°C , it is not possible to distinguish separate peaks, and the parameters of the single peak are plotted. Although this transition appears to be abrupt, a continuous increase in linewidth and slight decrease in frequency for the 101 cm^{-1} peak affects the convergence. The linewidth and intensity of the single peak (pink points) now reflect a broader, more intense lineshape.

In Fig. 10, the dominant component is the 414 cm^{-1} peak and its strong negative frequency shift with temperature of nearly 50 cm^{-1} . Its linewidth increases significantly, from 18 cm^{-1} at 30°C to $\approx 30\text{ cm}^{-1}$ at 300°C . The general trend of a decreasing center frequency with temperature of this peak, as well as an increasing linewidth, would suggest a similar peak convergence with the lower energy 350 cm^{-1} peak; however, a two-component fit to this multiplet (i.e., one peak near 480 and a second near 380 cm^{-1}) is inferior. The

linewidth increase of the 414 cm^{-1} is partly attributable to the collision with the lower-energy peak, as evidenced by the commensurate decrease in linewidth of the 350 cm^{-1} peak.

IV. DISCUSSION

We now consider both the 210°C thermodynamic phase transition and the 305°C structural phase transition separately in light of the measurements presented here.

To reiterate, previous authors have identified a λ -type phase transition beginning at 210°C and ending around 232°C on the basis of calorimetry [11,12,14,27]. A report by Momin *et al.* using differential scanning calorimetry also found the transition temperature to be $213 \pm 1^\circ\text{C}$, although it was incorrectly assigned to the $Amm2$ to $P\bar{6}2m$ transition [10].

Regarding structural measurements, Ackermann *et al.*, Hoekstra *et al.*, Siegel, and Grønbold measured the x-ray diffraction pattern of U_3O_8 *in situ* [3,7,9,28]. Those

TABLE III. Raman fit parameters for $\alpha\text{-U}_3\text{O}_8$ at 30 and 400°C .

Center cm^{-1}	30°C		400°C		
	Linewidth cm^{-1}	Amplitude a.u.	Center cm^{-1}	Linewidth cm^{-1}	Amplitude a.u.
87.0 ± 0.4	6.3 ± 0.4	145 ± 8	112.8 ± 1.7	5.7 ± 2.3	44 ± 39
101.7 ± 0.2	3.3 ± 0.2	80 ± 6	129.3 ± 0.4	5.5 ± 0.4	123 ± 9
123.8 ± 0.4	3.5 ± 0.3	85 ± 9	98.0 ± 1.7	9.7 ± 1.1	231 ± 37
134.7 ± 0.4	4.4 ± 0.4	118 ± 10	336.6 ± 4.8	7.7 ± 5.9	179 ± 100
343.4 ± 2.2	18.5 ± 3.9	262 ± 45	361.9 ± 17.7	27.6 ± 19.8	217 ± 15
414.2 ± 0.5	20.9 ± 0.8	1280 ± 90	476.7 ± 1.1	18.4 ± 1.9	477 ± 33
489.4 ± 1.0	22.6 ± 2.0	616 ± 43			

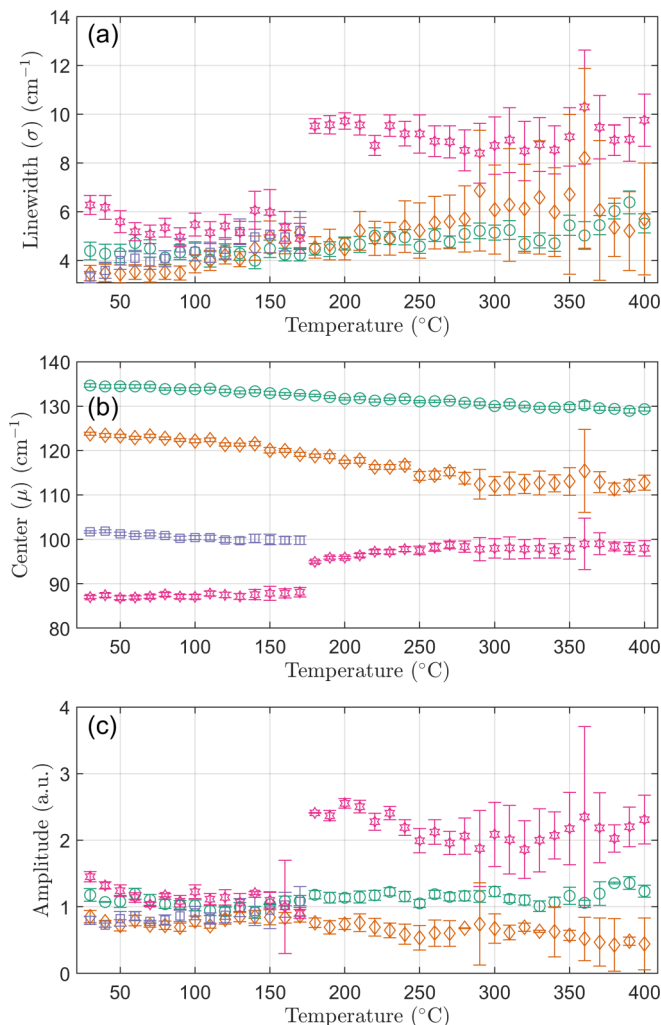


FIG. 9. (a) Gaussian linewidth, (b) center position, and (c) amplitude as a function of temperature for the quartet of modes in the 60–180 cm^{-1} band. Decomposition of the quartet into its constituent components shows that the two lower-energy modes converge at 180 $^{\circ}\text{C}$, with a commensurate broadening and intensity increase of the (single) peak above this temperature. The higher-energy modes show a softening and slight broadening with temperature.

measurements significantly disagreed about the precise temperature at which the structural phase transition was complete. The transition temperature is reported to be $350 \pm 10^{\circ}\text{C}$, 400°C , “about 400°C ” and [above 400°] by those authors, respectively [3,7,9,28]. None of these reports, however, noted special features in the diffraction measurements near 210 $^{\circ}\text{C}$. A careful look at the lattice constants reported by Ackermann *et al.* shows that they too demonstrate a discontinuity in the temperature derivatives of b and c near 210 $^{\circ}\text{C}$, but this was not discussed [3].

Noda *et al.* reported a kink in the temperature dependence of the phonon mean free path ($1/l_p$) at $\approx 197^{\circ}\text{C}$, which they noted was close to the starting point of the thermodynamic peak, but saw no discontinuities to correspond to the end point [29]. Electrical conductivity measurements show that a change in the derivative of conductivity occurs at exactly 210 $^{\circ}\text{C}$, suggesting an electronic contribution [14]. Naito *et al.* noted that a maximum in the unit cell volume appears at

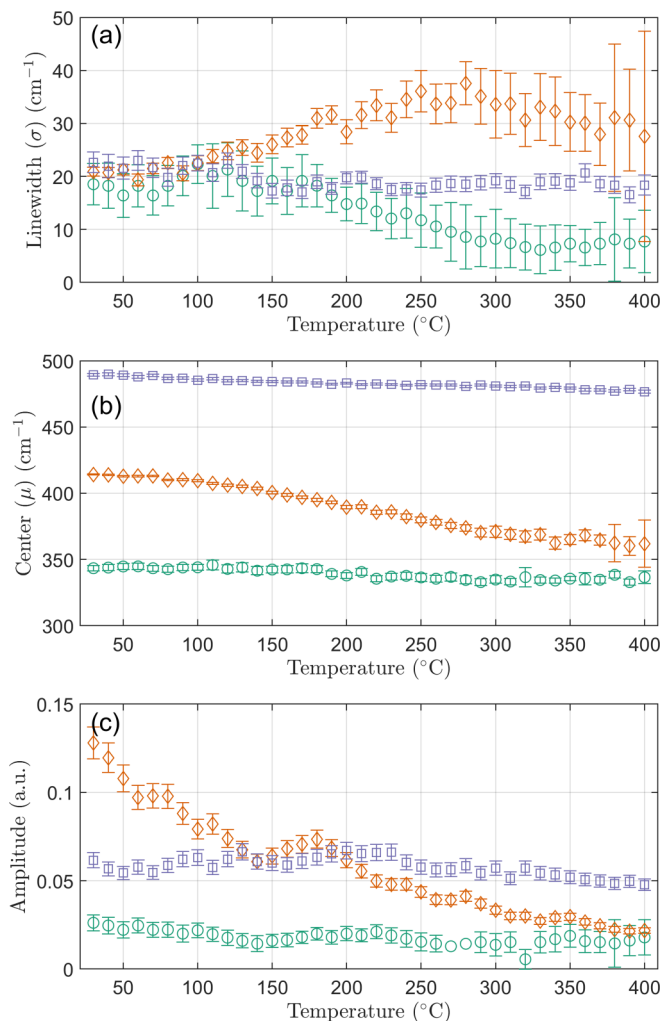


FIG. 10. (a) Gaussian linewidth, (b) center position, and (c) amplitude as a function of temperature for the triplet of modes in the 300–560 cm^{-1} band. In this band, the 418 cm^{-1} peak is the most intense and shows a significant softening from 414 to 360 cm^{-1} at 300 $^{\circ}\text{C}$. Its linewidth increases from 18 cm^{-1} at 30 $^{\circ}\text{C}$ to 30 cm^{-1} at 400 $^{\circ}\text{C}$, although the nearby modes have approximately temperature-independent linewidths and more slowly decreasing center frequencies.

210 $^{\circ}\text{C}$ [14]. They suggested the expansion of the c lattice parameter and contraction of the b lattice parameter was the result of a loss of order of the uranium oxidation state, going from well-defined U(V) and U(VI) at low temperature (below 210 $^{\circ}\text{C}$) to a fully disordered state in the hexagonal phase (above 305 $^{\circ}\text{C}$). A clear discontinuity in the temperature derivative of the unit cell volume (from negative to more negative) occurs in our data at 192 $^{\circ}\text{C}$. Although the unit cell volume shows more significant scatter than the b and c lattice constants themselves, 192 $^{\circ}\text{C}$ is firmly below 217 $^{\circ}\text{C}$, and there is no well-defined maximum in unit cell volume near 200 $^{\circ}\text{C}$. Therefore, we do not believe a maximum in unit cell volume is related to the onset of the order-to-disorder phase transition as has previously been suggested [14].

Subtle changes in the x-ray pattern can, however, be used to identify the order-to-disorder phase transition. The deriva-

tive of the b/c ratio (Fig. 5) shows a clear dip in the same temperature ranges identified by the heat capacity measurements. Based on Fig. 5 we propose a calorimetric transition temperature of $T_c = 210 \pm 3^\circ\text{C}$, which can easily be seen in the lattice constants themselves. We suggest that the b/c ratio is a surrogate quantity describing changes in the local U–O coordination environment. Additional measurements, such as a temperature-dependent measurement of the local structure via neutron or x-ray total scattering, could shed light on the local U–O rearrangements in this region. Especially given the role of electronic structure in the order-to-disorder transition, we speculate that changes in the local U–O coordination will adjust the crystal field potential and may be an important part of understanding the conductivity and the $Amm2$ to $P62m$ phase transition.

With regard to the main orthorhombic to hexagonal transition, the phase transition from $Amm2$ to $P\bar{6}2m$ requires a stretching and contraction of the in-plane lattice constants into a hexagonal configuration. The low- and high-temperature phases are nearly isomorphic, as evidenced by the closeness of the Bragg peaks in the $Amm2$ phase that become degenerate in $P\bar{6}2m$. This transition happens continuously, beginning essentially at room temperature and completing in the x-ray diffraction pattern around 300°C . Because it is so gradual, and between nearly isomorphic structures, it is not obvious exactly where the transition occurs. Using the same multipeak fitting approach we used for the Raman peaks, we fit the sets of Bragg peaks in Fig. 3 to either one or two Gaussian peaks and found that a two-peak fit (i.e., $Amm2$) was superior up to 305°C and inferior to a single peak ($P\bar{6}2m$) based on the Akaike information criteria above 305°C for all sets [30]. We suggest a structural transition temperature, T_s , value of $305 \pm 5^\circ\text{C}$. Compared to previous determinations, all previous authors agree that U_3O_8 is orthorhombic at low temperature and undergoes a hexagonal phase transition at elevated temperature, but the precise determination of that temperature has produced values from $305 \pm 5^\circ\text{C}$ (this work) up to 400°C (Hoekstra *et al.*) [3,7,9,28]. One barrier to the convergence of these literature values apparently is the relatively poor temperature resolution of previous measurements (apparently no better than 40°C).

The most recent assessment, based on calorimetric data, places the orthorhombic to hexagonal phase transition at $297 \pm 5^\circ\text{C}$, in concordance with our determination, as reported in Table IV [14,27,29]. To our knowledge, our x-ray diffraction measurement is the first to assert the same temperature as the thermodynamic data for this phase transition and suggests there is no fundamental disagreement between the methods.

TABLE IV. Phase transition temperatures in $\alpha\text{-U}_3\text{O}_8$ as determined from x-ray diffraction.

Transition	Temperature ($^\circ\text{C}$)	Ref. (via calorimetry)
T_c U order-to-disorder	210 ± 3	210 [12]
T_s $Amm2$ to $P\bar{6}2m$	305 ± 5	297 ± 5 [12,14,27,31]

TABLE V. Frequency shifts for select Raman modes.

$\omega_0 - 30^\circ\text{C}$ cm^{-1}	$\frac{d\omega}{dV}$ $\text{cm}^{-1}\text{\AA}^{-3}$	Polarization	$\frac{d\omega}{dl}$ $\text{cm}^{-1}\text{\AA}^{-1}$
92	-10.8 ± 1.2	b	-46.0 ± 2.2
124	19.7 ± 1.9	c	-143.9 ± 6.1
135	8.3 ± 0.3	c	-60.7 ± 0.8
343	18.1 ± 4.2	c	-131.5 ± 25.6
414	88.8 ± 19.0	c	-644.6 ± 22.3
489	15.5 ± 3.1	c	-116.6 ± 10.6

The most notable features of the Raman spectra are the very large negative shifts in phonon frequency for a number of modes. Although the 414 cm^{-1} mode shift is the most obvious, the 124, 135, 343, 489, and 807 cm^{-1} modes display negative temperature dependence as well. What is surprising about this result is that the unit cell volume in those temperatures is *decreasing*. Again, a general expectation would be that phonon frequencies should decrease with increasing lattice volume simply because of the increase in separation between atoms. Based on thermal conductivity measurements, a kink in the phonon mean-free path is observed at 167°C , and this temperature corresponds somewhat to the onset of significant linewidth broadening of the 414 cm^{-1} mode and its thermal energy [29]. The 414 cm^{-1} mode in particular is interesting because of its extreme redshifting, nearly 50 cm^{-1} in the relevant temperatures, and its polarization. This mode may play a role in facilitating the orthorhombic to hexagonal phase transition, either by driving the tetragonal distortion or by following it.

In Fig. 11 we plot the frequency of select Raman modes against specific lattice constants. The comparison to the set of all lattice constants and unit cell volume (Fig. 4) shows that the vibrational frequencies are *not* correlated with the unit cell volume. In fact, the apparently contradictory fact is that the frequency of all Raman modes in Fig. 11, except the 92-cm^{-1} mode, show a decreasing frequency with decreasing unit cell volume. This is quantified in Table V, which shows positive values of $\frac{d\omega}{dV}$ (i.e., wrong sign). However, plotted against the c lattice constant, $\frac{d\omega}{dc}$ is negative. Because a decreasing frequency with decreasing volume is rather unusual, we hypothesize that the 124, 135, 343, 414, and 489 cm^{-1} phonons are polarized along the c axis, and the 92 cm^{-1} is polarized along b , and display normal response to change in dimension. This hypothesis could be verified with polarized Raman spectroscopy, or with theoretical calculations that could determine the phonon polarization and response to tetragonal strain. Some density functional theory calculations exist, but the mixed valence of U_3O_8 evidently requires the use of hybrid functionals and spin-orbit corrections to find the correct electronic state [32–34]. Computing the vibrational frequencies is an additional computational expense. The data presented here cannot definitively eliminate the possibility of exotic phonon softening under unit cell contraction, which could perhaps be done with the assistance of theory. The a lattice constant also decreases with temperature, but the change from 40 to 440°C (0.9 pm) is about an order of magnitude smaller than the change in c ,

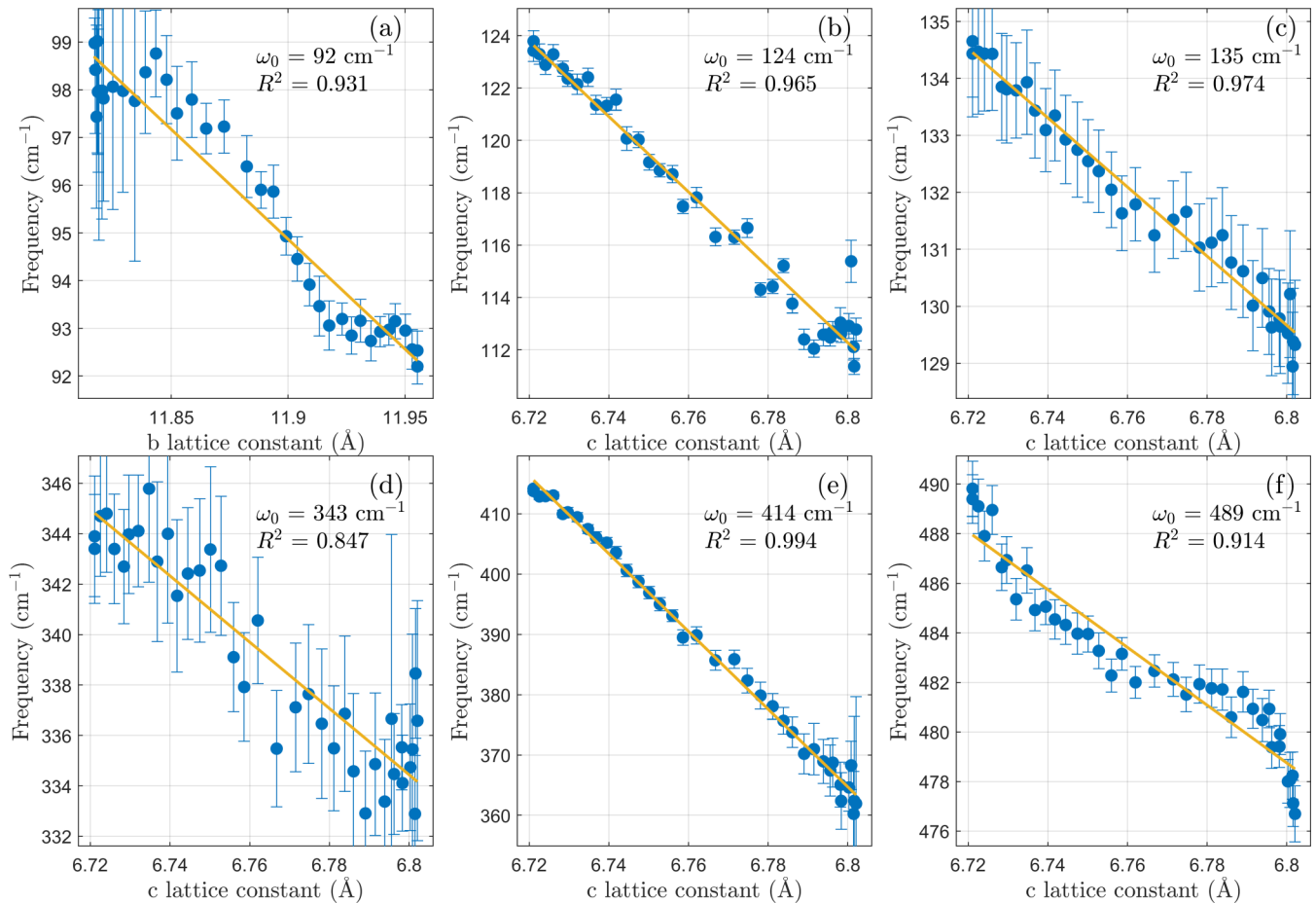


FIG. 11. Fitted Raman frequency vs. selected lattice constant for six specific Raman modes. Because the lattice constants, determined from x-ray diffraction, and the frequencies, from Raman spectroscopy, were collected on distinct temperature grids, the lattice constants were interpolated to the coarser temperature set. Plotted in this way, the negative relation between frequency and lattice constant indicates a decrease in frequency with increasing lattice constant—a normal behavior. Note that panel (a), for the 92 cm^{-1} mode, is correlated to the negative slope to the b lattice constant, instead of the c lattice constant as in panels (b)–(f). Although it is clear that there are linear correlations between frequency and lattice constant, a comparison to Fig. 4 shows that this result is nontrivial. Uncertainty in the lattice constants is smaller than the size of data points. ω_0 corresponds to the frequency at 30°C . The yellow lines are linear fits, and corresponding R^2 factors are given.

and it could not be discerned whether it correlated strongly with other modes. Modes at 220 and 244 cm^{-1} showed only weak correlation with the lattice constants—they may be isotropic or polarized along a . The 807 cm^{-1} was weakly correlated to c , although with high uncertainty. To wit, a simple comparison of frequency versus unit cell volume would indicate an unusual phonon softening with decreasing unit cell volume, but properly accounting for the anisotropic lattice expansion suggests a more plausible connection between specific Raman active phonons and specific crystallographic polarizations.

Given the importance of phonons at the relevant temperature and the conductivity being driven by an electron hopping mechanism, time-dependent valence configurations [i.e., each site oscillates between U(V) and U(VI) with a timescale t_{hop}] should be considered. First, it should be clarified that t_{hop} in this context must be shorter than a reordering time t_{ord} representing the time required for the ions to respond to an instantaneous change in electron density; otherwise, it is equivalent to the time-independent case. An estimate of this

reordering time would be the characteristic phonon period, approximately 100 fs . The consequences of a time-dependent valence configuration would be a contribution to the electrical conductivity due to site-to-site hopping, a lack of superlattice Bragg reflections, and an increase in the electronic contribution to the specific heat. Separating the time-dependent from time-independent oxidation state pictures would set a bound on t_{hop} . If U oxidation oscillations occur by a mechanism of electron site-to-site hopping, hops may be optically excitable. Previously, we did not observe dispersive behavior in Raman spectra that could suggest inelastic photons of nonvibrational origin between 100 and 1200 cm^{-1} , but the cross-section for optical excitation may be very low, the activation energy may be below or above the experimental limits, and the dispersion may be rather weak given the small momentum transfer of optical excitation [18]. Site-to-site hopping between U sites separated by 3.75 \AA would be directly observable with inelastic neutron scattering if the excitation energy lies within the neutron kinematic restraints for 1.67 \AA^{-1} , and perhaps indirectly observable at higher energies.

V. CONCLUSION

We measured the temperature-dependent x-ray diffraction pattern and Raman spectra of stoichiometric U_3O_8 through the order-to-disorder phase transition and the structural phase transition. In the x-ray, we show a gradual convergence of Bragg peaks associated with the $Amm2$ structure to the higher symmetry $P\bar{6}2m$ structure. This convergence is complete at $T_s = 305 \pm 5$ °C. The lattice expansion in the $Amm2$ phase is anisotropic, with the out-of-plane a and in-plane b lattice constants monotonically decreasing with temperature and the in-plane c lattice constant increasing. The unit cell volume, however, demonstrates a peculiar temperature dependence, being nearly temperature independent until 200 °C, then decreasing to a minimum near 325 °C, slightly above the orthorhombic to hexagonal phase transition. A detailed analysis of the structure shows that there are specific quantities in the bulk structure that correspond to the calorimetric peaks previously identified as the onset of the order-to-disorder transition. One of these quantities is the b/c ratio, whose derivative shows a well-defined minimum value precisely between 210 and 237 °C, the onset and offset temperatures identified via calorimetry [12]. Its onset is $T_c = 210 \pm 3$ °C. This feature is suggestive of local U–O rearrangements associated with the order-to-disorder transition and warrants additional study.

Long scans of the specimen at elevated temperature (in the hexagonal phase) allow us to place a maximum value on the scattering power of a potential superlattice Bragg peak with d -spacing less than 16 Å to below $1 e^-$. This measurement effectively eliminates the possibility of time-independent, ordered U(V) and U(VI) sites in the hexagonal phase.

Raman spectra indicate strong shifts in phonon frequencies at elevated temperature. The most apparent feature is a

–54 cm^{-1} shift in the 414 cm^{-1} mode from 30 to 400 °C, but a detailed accounting shows that five of the major phonon bands demonstrate phonon softening and one, near 92 cm^{-1} , hardens with increasing temperature. Meanwhile, in the same temperature regions, the unit cell volume reaches a *minimum* near 332 °C. The phonon softening with decreasing unit cell volume can be rectified by noting the strong correlation between these phonon frequencies and specific lattice constants, notably the c lattice constant increases significantly below 332 °C despite the monotonically decreasing unit cell volume.

The Department of Energy will provide public access to these results of federally sponsored research in accordance with the DOE Public Access Plan in Ref. [35]. A portion of this work was supported by the US Department of Energy National Nuclear Security Administration.

ACKNOWLEDGMENTS

The authors would like to thank Z. Brubaker (ORNL) and D. Duckworth (ORNL) for a critical reading of the manuscript. This manuscript has been authored by UT-Battelle, LLC under Contract No. DE-AC05-00OR22725 with the U.S. Department of Energy. The United States Government retains and the publisher, by accepting the article for publication, acknowledges that the United States Government retains a nonexclusive, paid-up, irrevocable, world-wide license to publish or reproduce the published form of this manuscript, or allow others to do so, for United States Government purposes.

-
- [1] R. J. McEachern, J. W. Choi, M. Kolár, W. Long, P. Taylor, and D. D. Wood, Determination of the activation energy for the formation of U_3O_8 on UO_2 , *J. Nucl. Mat.* **249**, 58 (1997).
 - [2] G. C. Allen and N. R. Holmes, A mechanism for the UO_2 to α - U_3O_8 phase transformation, *J. Nucl. Mat.* **223**, 231 (1995).
 - [3] R. J. Ackermann, A. T. Chang, and C. A. Sorrell, Thermal expansion and phase transitions of the U_3O_{8-z} phase in air, *J. Inorg. Nucl. Chem.* **39**, 75 (1977).
 - [4] K. O. Kvashnina, S. M. Butorin, P. Martin, and P. Glatzel, Chemical State of Complex Uranium Oxides, *Phys. Rev. Lett.* **111**, 253002 (2013).
 - [5] G. Leinders, R. Bes, J. Pakarinen, K. Kvashnina, and M. Verwerft, Evolution of the uranium chemical state in mixed-valence oxides, *Inorg. Chem.* **56**, 6784 (2017).
 - [6] R. E. Rundle, N. C. Baenziger, A. S. Wilson, and R. A. McDonald, The structures of the carbides, nitrides and oxides of uranium, *J. Am. Chem. Soc.* **70**, 99 (1948).
 - [7] S. Siegel, The crystal structure of trigonal U_3O_8 , *Acta. Cryst.* **8**, 617 (1955).
 - [8] V. V. Rachev, L. M. Kovba, and E. A. Ippolitova, A contribution to the study of the UO_2 – UO_3 system, *Dokl. Akad. Nauk. SSSR* **159**, 1371 (1964).
 - [9] H. R. Hoekstra, S. Siegel, L. H. Fuchs, and J. J. Katz, The uranium-oxygen system: $UO_{2.5}$ to U_3O_8 , *J. Phys. Chem.* **59**, 136 (1954).
 - [10] A. C. Momin, V. V. Deshpande, and M. D. Karkhanavala, Phase transition studies of α -, β -, and δ - U_3O_8 , *J. Nucl. Mat.* **49**, 98 (1973).
 - [11] H. L. Girdhar and E. F. Westrum, λ -type thermal anomaly in triuranium octaoxide at 482.7 K. *J. Chem. Eng. Data* **13**, 531 (1968).
 - [12] H. Inaba, H. Shimizu, and K. Naito, Lambda-type heat capacity anomalies in U_3O_8 , *J. Nucl. Mat.* **64**, 66 (1977).
 - [13] T. Ishii, K. Naito, and K. Oshima, Electrical conductivity study on phase transitions in U_3O_8 , *J. Nucl. Mat.* **35**, 335 (1970).
 - [14] K. Naito, T. Tsuji, and F. Ohya, Phase transitions in U_3O_{8-z} : I, Electrical conductivity measurement, *J. Nucl. Mat.* **114**, 136 (1983).
 - [15] I. S. Butler, G. C. Allen, and N. A. Tuan, Micro-Raman spectrum of triuranium octoxide, U_3O_8 , *Appl. Spectrosc.* **42**, 901 (1988).
 - [16] E. A. Stefaniak, A. Alseccz, I. E. Sajò, A. Worobiec, Z. Máthé, S. Török, and R. V. Grieken, Recognition of uranium oxides in soil particulate matter by means of μ -Raman spectrometry, *J. Nucl. Mat.* **381**, 278 (2008).

- [17] G. C. Allen, I. S. Butler, and N. A. Tuan, Characterisation of uranium oxides by micro-Raman spectroscopy, *J. Nucl. Mat.* **144**, 17 (1987).
- [18] A. Miskowiec, J. L. Niedziela, T. L. Spano, M. W. Ambrogio, S. Finkeldei, R. Hunt, and A. E. Shields, Additional complexity in the Raman spectra of U_3O_8 , *J. Nucl. Mater.* **527**, 151790 (2019).
- [19] G. Gouadec and P. Colomban, Raman spectroscopy of nano-materials: How spectra relate to disorder, particle size, and mechanical properties, *Prog. Cryst. Growth Ch.* **53**, 1 (2006).
- [20] B. H. Toby, EXPGUI, a graphical user interface for GSAS, *J. Appl. Crystal.* **34**, 210 (2001).
- [21] A. Miskowiec, "PeakFitGUI." Computer software. September 04, 2019. <https://code.ornl.gov/gxm/peakfitgui>, doi: 10.11578/dc.20190904.1.
- [22] M. Newville, R. Otten, A. Nelson, A. Ingargiola, T. Stensitzki, D. Allan, A. Fox, F. Carter, Michał, D. Pustakhod, Glenn, Y. Ram, MerlinSmiles, C. Deil, Stuermer, A. Beelen, O. Frost, gasquev, A. L. R. Hansen, A. Stark, T. Spillane, S. Caldwell, A. Polloreno, andrewhannum, J. M. Borreguero, J. Fraine, deep 42-thought, B. F. Maier, B. Gamari, and A. Almarza, *lmfit/lmfit-py* 0.9.13, (2019), doi: 10.5281/zenodo.2620617.
- [23] P. H. C. Eilers and H. F. M. Boelens, *Baseline Correction with Asymmetric Least Squares Smoothing*, Report (Leiden University Medical Center, Leiden, Netherlands, 2005).
- [24] B. O. Loopstra, Neutron diffraction investigation of U_3O_8 , *Acta. Cryst.* **17**, 651 (1964).
- [25] B. O. Loopstra, The phase transition of α - U_3O_8 at 210° C, *J. Appl. Cryst.* **3**, 94 (1970).
- [26] M. L. Palacios and S. H. Taylor, Characterization of uranium oxides using in situ micro-Raman spectroscopy, *Appl. Spectrosc.* **54**, 1372 (2000).
- [27] D. Labroche, O. Dugne, and C. Chatillon, Thermodynamic properties of the O-U system II – Critical assessment of the stability and composition range of the oxides UO_{2+x} , U_4O_{9-y} and U_3O_{8-z} , *J. Nucl. Mat.* **312**, 50 (2003).
- [28] F. Grønvold, High-temperature x-ray study of uranium oxides in the UO_2 - U_3O_8 region, *J. Inorg. Nucl. Chem.* **1**, 357 (1955).
- [29] Y. Noda and K. Naito, The thermal conductivity of U_3O_{8-z} from 200 to 750 K, *J. Nucl. Mat.* **80**, 102 (1979).
- [30] H. Akaike, Fitting autoregressive models for prediction, *Ann. I. Stat. Math.* **21**, 243 (1969).
- [31] K. Naito, H. Inaba, and S. Takahashi, Phase transitions in U_3O_{8-z} : I, heat capacity measurements, *J. Nucl. Mat.* **110**, 317 (1982).
- [32] J. I. Ranasinghe, L. Malakkal, E. Jossou, B. Szpunar, and J. A. Szpunar, Comprehensive study on the electronic and optical properties of α - U_3O_8 , *Comput. Mater. Sci.* **171**, 109264 (2020).
- [33] N. A. Brincat, S. C. Parker, M. Molinari, G. C. Allen, and M. T. Storr, Density functional theory investigation of the layered uranium oxides U_3O_8 and U_2O_5 , *Dalton Trans.* **44**, 2613 (2015).
- [34] Y. Yun, J. Ruzs, M. T. Suzuki, and P. M. Oppeneer, First-principles investigation of higher oxides of uranium and neptunium: U_3O_8 and Np_2O_5 , *Phys. Rev. B* **83**, 075109 (2011).
- [35] <http://energy.gov/downloads/doc-public-access-plan>.